Lawrence Berkeley National Laboratory
Recent Work

Title
Initial Steps in Forming the Electrode-Electrolyte Interface: H_2O Adsorption and Complex Formation on the Ag(111) Surface from Combining Quantum Mechanics Calculations and Ambient Pressure X-ray Photoelectron Spectroscopy.

Permalink
https://escholarship.org/uc/item/3k34t7zv

Journal
Journal of the American Chemical Society, 141(17)

ISSN
0002-7863

Authors
Qian, Jin
Ye, Yifan
Yang, Hao
et al.

Publication Date
2019-05-01

DOI
10.1021/jacs.8b13672

Peer reviewed

eScholarship.org Powered by the California Digital Library
University of California

Initial Steps in Forming the Electrode−Electrolyte Interface: H_2O Adsorption and Complex Formation on the Ag(111) Surface from Combining Quantum Mechanics Calculations and Ambient Pressure X-ray Photoelectron Spectroscopy

Jin Qian,[†,‡,#] Yifan Ye,[§,∥,⊥,#] Hao Yang,[‡] Junko Yano,[*,§] Ethan J. Crumlin,[*,∥,⊥] and William A. Goddard III[*,†,‡]

[†]Joint Center for Artificial Photosynthesis, California Institute of Technology, Pasadena, California 91125, United States
[‡]Materials and Process Simulation Center, California Institute of Technology, Pasadena, California 91125, United States
[§]Joint Center for Artificial Photosynthesis, Lawrence Berkeley National Laboratory, Berkeley, California 94720, United States
[∥]Advanced Light Source, Lawrence Berkeley National Laboratory, Berkeley, California 94720, United States
[⊥]Chemical Sciences Division, Lawrence Berkeley National Laboratory, Berkeley, California 94720, United States

ABSTRACT: The interaction of water with metal surfaces is at the heart of electrocatalysis. But there remain enormous uncertainties about the atomistic interactions at the electrode−electrolyte interface (EEI). As the first step toward an understanding of the EEI, we report here the details of the initial steps of H_2O adsorption and complex formation on a Ag(111) surface, based on coupling quantum mechanics (QM) and ambient-pressure X-ray photoelectron spectroscopy (APXPS) experiments. We find a close and direct comparison between simulation and experiment, validated under various isotherm and isobar conditions. We identify five observable oxygen-containing species whose concentrations depend sensitively on temperature and pressure: chemisorbed O* and OH*, H_2O* stabilized by hydrogen bond interactions with OH* or O*, and multilayer H_2O*. We identify the species experimentally by their O 1s core-level shift that we calculate with QM along with the structures and free energies as a function of temperature and pressure. This leads to a chemical reaction network (CRN) that we use to predict the time evolution of their concentrations over a wide range of temperature (298−798 K) and pressure conditions (10^{-6}−1 Torr), which agree well with the populations determined from APXPS. This multistep simulation CRN protocol should be useful for other heterogeneous catalytic systems.

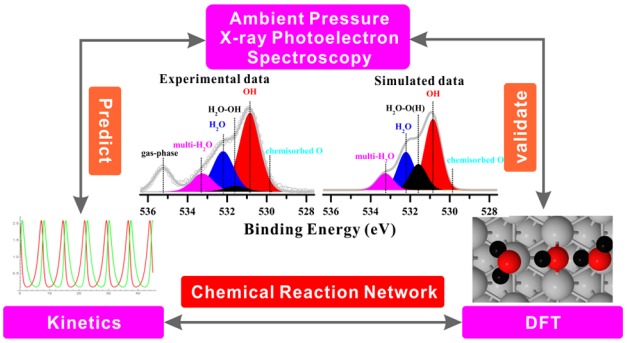

1. INTRODUCTION

Ubiquitous in electrocatalytic systems are heterogeneous metal surfaces or metal nanoparticles interacting with a H_2O-based solvent. Classical examples include CO_2 reduction reaction (CO_2RR) using Cu, Ag, and Au;[2−5] oxygen evolution reaction (OER) using Ru, Ir, Pt, and IrO_2;[6,7] and water−gas shift (WGS) reaction using ceria-supported Pd, Pt, Rh, and Cu.[8,9] To systematically improve the performance of these processes requires understanding of the interface between the H_2O phase and the transition metal surface. However, at a fundamental level, the link between theory and experiments is lacking.[10]

To determine the atomistic nature of this interface, we recently combined ambient-pressure X-ray photoelectron spectroscopy (APXPS) and quantum mechanics (QM) to elucidate the initial steps of CO_2 reduction on a Cu(111) surface at 298 K and ∼1 Torr pressure, where we found that water plays a significant role: binding to a surface Cu^+ site stabilized by a subsurface O to form a hydrogen bond (HB) that stabilizes bent CO_2 (*b*-CO_2), the intermediate in the reduction mechanism, which accepts H atoms from surface water, leading to the reaction sequence[11]

$$l\text{-}CO_2 + H_2O \rightarrow b\text{-}CO_2 + H_2O \rightarrow HCO_2 + OH \rightarrow CO + 2OH$$

Similar experiments on Ag(111) showed that surface oxygen, O*, activates CO_2 to form a carbonic acid species, $O{=}CO_2^{\delta-}$, which stabilizes up to four surface H_2O, leading subsequently to protonation. It is likely that related surface reactions play a role in such water-involved reactions, such as the WGS reaction and steam reforming reactions in addition to CO_2RR. This makes characterizing the stability and concentration of oxygen-containing species formed upon water adsorption essential to

understanding of the first steps of adsorption, reaction, and selectivity to reduction products. Given the maximum water pressure that could be explored for this study, this work is directly crucial to gas-phase catalytic process. Due to the explicit introduction of water molecule and related oxygen-containing species, and a saturation observed from 0.03 to 0.1 Torr, the relevance to liquid−solid interface could be implied.

Previous experimental methods employed to provide a macroscopic picture for water adsorption on metal surfaces include low-temperature ultra-high-vacuum-based experiments,[12,13] temperature-programmed desorption (TPD) spectroscopy,[14−16] work function measurements,[17] and ultraviolet or X-ray photoelectron spectroscopy (UPS, XPS).[18,19] Among these experimental methods, XPS provides the sensitivity and resolution needed to distinguish oxygen-containing surface species (surface O atom, subsurface oxygen atom, water clusters, or byproducts of H_2O decomposition such as OH) by measuring the O 1s core electron binding energy (BE). Often, the XPS peak assignments are based on a combination of database,[20] previous publications, and chemical insight. In this work, we bring theory and experiments together, adding another layer of clearance and cross-validation. We created the following protocol to clearly and correctly reflect the chemistry:

Screening based on QM calculations of stable surface adsorbates' free energy G, under experimental conditions of temperature and pressure

Assignment of core-level peak of stable surface species based on QM core-level calculation

Network: chemical reaction network (CRN) kinetics simulation of the concentration of each surface species

Deconvolution of XPS data using the QM core-level shifts

Sanity check: cross-validation of experiment and theory by matching the intensity of deconvoluted peaks with the concentrations predicted from the CRN

The key advantage of this new SANDS protocol is that both the peak position and peak intensity of multiple species in a complex system can be predicted *ab initio*, without empirical input. We predict the XPS spectrum from core-level QM calculations along with structures' free energies, then the kinetics of the CRN, and then populations compared with experiment. These predictions are cross-validated directly with the APXPS. Every step in the SANDS protocol is based on QM electronic structure, thermodynamics, and kinetics. We expect this protocol to be easily transferable to other catalytic scenarios.

We demonstrate this procedure by disentangling the complex landscape of H_2O adsorption on Ag(111) at 298 K and various pressures, as shown in section 3.3, and then we predict the concentrations as a function of pressure and temperature, which are tested and validated by experiments in section 3.4. This leads finally to predicting the overall concentration landscape from room temperature to 500 °C, with pressure from 10^{-6} to 1 Torr, in section 3.4.3.

2. METHODS

2.1. Theoretical Method. *2.1.1. DFT Calculation.* All calculations, including geometric optimization, free energy correction, and O 1s core-level shift, were carried out with the Vienna Ab-initio Simulation Package (VASP).[21] We used the Perdew−Burke−Ernzerhof (PBE) formulation of the generalized gradient approximation (GGA) exchange-correlation functional using the projector-augmented (PAW) method and including the D3 (Grimme, Becke, and Johnson)[22] empirical corrections for long-range London dispersion.[23] We used a plane-wave basis set cutoff of 600 eV. We sampled reciprocal space by a Γ-centered Monkhorst−Pack scheme with 3×3×1 for all calculations.

The PBE-D3(BJ) level of DFT leads to a calculated lattice parameter of a = 4.012 Å for the bulk Ag structure at 0 K, taking into account of the linear thermal expansion coefficient of Ag (19×10^{-6}/K), the lattice parameter would be 4.035 Å at T= 298 K, slightly smaller than the experimental value 4.085 Å at 298 K.[24] Because D3 does not address the screening in metal well,[25] we used experimental lattice parameter 4.085 Å to construct a two-dimensional periodic slab with four layers of Ag (111) atoms each of which consists of a (4×4) unit cell (16 surface Ag per cell) in order to capture the strain energy of thermal expansion under experimental condition. We found that using D3 lattice parameter vs using experimental lattice parameter does not shift the relative adsorption energy, shown in Table S2. We include 25 Å of vacuum in the z direction to minimize possible interactions between the replicated cells. Dipole correction is included. The top two layers are relaxed while the bottom layers are kept fixed. The O 1s core level relative to gas-phase H_2O was used to the position of the center of the peak. More detailed discussion of core-level shift calculation is included in the Supporting Information.

Calculations for the gas-phase molecules used the same level PBE functional (as implemented in Jaguar) with the D3 empirical correction for London dispersion.[22] Jaguar[26] has postprocessing of translational, rotational, vibrational entropy and enthalpy implemented described in the Supporting Information. Consistency between frequency modes generated in Jaguar, VASP, and experiments is included in Table S3.

We assumed a roto-translational model for adsorption of molecules, as described in ref 27, to obtain the total free energy, $G = H - TS$, for the gas molecules at temperature T, we add to the DFT electronic energy (E), the zero-point energy (ZPE) from the vibrational levels (described as simple harmonic oscillators), and the specific heat corrections in the enthalpy from 0 to T. The entropy (S) is evaluated from the same vibrational levels. To correct the free energy for pressure, we assume an ideal gas and add $RT \ln(P_2/P_1)$ with a reference pressure of P = 1 atm.

2.1.2. CRN Kinetics Simulation. CRN theory has attracted surging interests among biologists, mathematicians, computer scientists, and chemists. Interesting works in bulk reactor,[28] molecular biology and DNA programming,[29] etc. benefit from the CRN theory. It aims at relating the topological features of a system using a nonlinear, parameter-dependent network of ordinary differential equations.[30] From an abstract level, individual chemical reactions happening at the rate K_{ij} are denoted as

$$\sum_{j\in S} \alpha_{ij} S_j \overset{K_{ij}}{\leftrightarrow} \sum_{j\in S} \beta_{ij} S_j$$

where $S\{S_j \in S\}$ is a complete set of chemical species and α_{ij}, β_{ij} are non-negative integers that are directly related to the stoichiometry of the reactants and products. Thus, we can arrange the stoichiometry factors into an $n_s \times n_r$ matrix, where n_s stands for the number of chemical species and n_r stands for the number of reactions, and then we can assign a rate constant.

We relate the QM formation free energies to the reaction rate constant K, using the Arrhenius equation $K = k_B \frac{T}{h} \exp\left(\frac{dG}{k_B T}\right)$. Thus, for the reaction A + B → C, $\frac{d[C]t}{dt} = [A]t[B]tK$. As the reaction proceeds, products from the previous reaction serve as the reactants for the subsequent reaction. Our proposed CRN is shown in section 3.2. We obtained numerical solutions for the CRN[31] at equilibrium state in terms of the population for each species for the (4×4) unit cell. The predicted population of each species is then used to determine the height of XPS peak (the full width at half-maximum (fwhm) is determined as 0.8 eV, for visualization purposes.)

2.2. Experimental Methods. Ambient pressure XPS measurements were performed at Beamline 9.3.2 of the Advanced Light Source, Lawrence Berkeley National Laboratory.[32] The pristine Ag surface was prepared *in situ* in the vacuum chamber by repeated argon sputtering (2 keV, 60 min) and vacuum annealing (900 K, 60 min). As the (111) surface is closest packed, energetically the most favorable facet for fcc metals (such as Ag and Cu), experimental evidence indicates that Ag

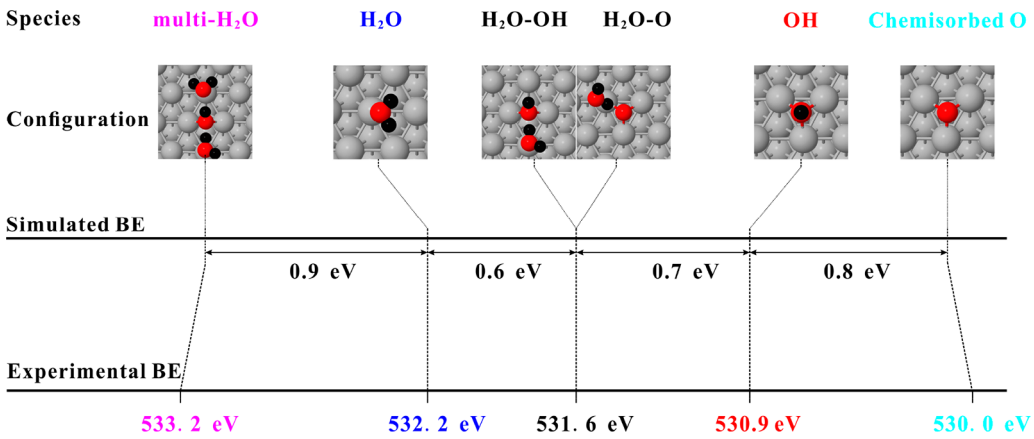

Figure 1. Predicted O 1s core-level shift vs experimental binding energy (BE). Six possible oxygen-containing surface species with five groups of BE are identified using DFT. The calculated O 1s core-level shift are compared directly with experimental BE. From high BE to low BE, these species are multilayer H_2O^*, H_2O^*, H_2O^*---hb (including H_2O^*---OH and H_2O^*---O), OH*, and chemisorbed O*. This excellent comparison validates the accuracy of the calculations-based interpretations of the experiment.

(and Cu) catalyst treated with high temperature exposes this facet.[1,33,34] Thus, our simulations assumed the Ag(111) surface to correlate with the experimental observations on vacuum annealed polycrystalline Ag surface.

For the isothermal comparisons, we considered the H_2O partial pressure from 10^{-6} to 0.1 Torr. For the isobaric comparisons, we heated the sample from 298 to 573 K while keeping the H_2O partial pressure at 0.1 Torr. The purities of the dosing gases (H_2O) were *in situ* monitored by a conventional quadrupole mass spectrometer to ensure no additional gas cross-contamination.

The XPS spectra were collected at an incident photon energy of 670 eV, in the following order: a low-resolution survey with a binding energy of 600 eV to −5 eV, then high-resolution scans of the O 1s. The carbon contamination is minor (estimated to be at most ~0.05 ML). For the completion of this work, the extreme scenario of such contamination is discussed and analyzed in the Supporting Information. The inelastic mean free path (IMFP) for the photoelectrons was below 0.9 nm for all the spectra collected. For each condition, samples were equilibrated for at least 30 min before measurements. By taking spectra at different sample spots and comparing spectra before and after beam illumination for 2 h, we found beam damage on the sample is negligible during the measurements.

3. RESULT AND DISCUSSION

3.1. Adsorption Geometry and O 1s Binding Energy. Six species were investigated using DFT, with their adsorption geometries shown in Figure 1 (H atoms are black circles, O atoms are red circles, and Ag substrates are silver circles). We found that isolated OH* and O* adsorb at fcc three-fold sites, while isolated H_2O^* adsorbs at the on-top site, consistent with previous calculations.[35] We find that H_2O molecules are stabilized by forming hydrogen bonds to surface O* or OH*, which we denote as H_2O^*---hb. We find that multilayer H_2O molecules can be stabilized by OH*. To be specific, we calculated that, in H_2O−OH, the O 1s level in OH is the same as that in OH* alone, whereas in H_2O−O, the O 1s level in O is the same as that in O* alone. Thus, the concentration of species H_2O^*---hb is calculated explicitly.

The O 1s core level of each species is calculated using DFT with the relative values compared with experiment in Figure 2, below. The stability of these species as a function of temperature and pressure is shown and discussed in detail in sections 3.2 and 3.4.

3.2. Proposed Chemical Reaction Network. We propose a CRN consisting of 12 reactions, where "*" denotes a surface site or adsorbed species, "g" represents the gas phase, and "---hb" indicates a hydrogen bond formed with neighboring O or OH. Two extreme pressure conditions (10^{-6} Torr and 0.1 Torr under room temperature) are chosen as representatives. G_1 is the free energy for 0.1 Torr and G_2 is the free energy for 10^{-6} Torr. The favorable reactions with negative energy are highlighted in boldface.

adsorption

$$O^* + H_2O_g + * \rightarrow O^* + H_2O^*\text{---hb}, \quad \mathbf{G_1 = -0.28\ eV},\ G_2 = 0.02\ \text{eV} \tag{1}$$

adsorption

$$OH^* + H_2O_g + * \rightarrow OH^* + H_2O^*\text{---hb}, \quad \mathbf{G_1 = -0.14\ eV},\ G_2 = 0.16\ \text{eV} \tag{2}$$

reaction

$$O^* + H_2O^*\text{---hb} \rightarrow 2OH^*, \quad \mathbf{G_1 = -0.32\ eV},\ \mathbf{G_2 = -0.32\ eV} \tag{3}$$

diffusion

$$H_2O^*\text{---hb} + OH^* \rightarrow H_2O^* + OH^*, \quad G_1 = 0.28\ \text{eV},\ G_2 = 0.28\ \text{eV} \tag{4}$$

diffusion

$$H_2O^*\text{---hb} + O^* \rightarrow H_2O^* + O^*, \quad G_1 = 0.41\ \text{eV},\ G_2 = 0.41\ \text{eV} \tag{5}$$

desorption

$$H_2O^* \rightarrow H_2O_g + *, \quad \mathbf{G_1 = -0.14\ eV},\ \mathbf{G_2 = -0.43\ eV} \tag{6}$$

adsorption

$$H_2O_g + * \rightarrow H_2O^*, \quad G_1 = 0.14\ \text{eV},\ G_2 = 0.43\ \text{eV} \tag{7}$$

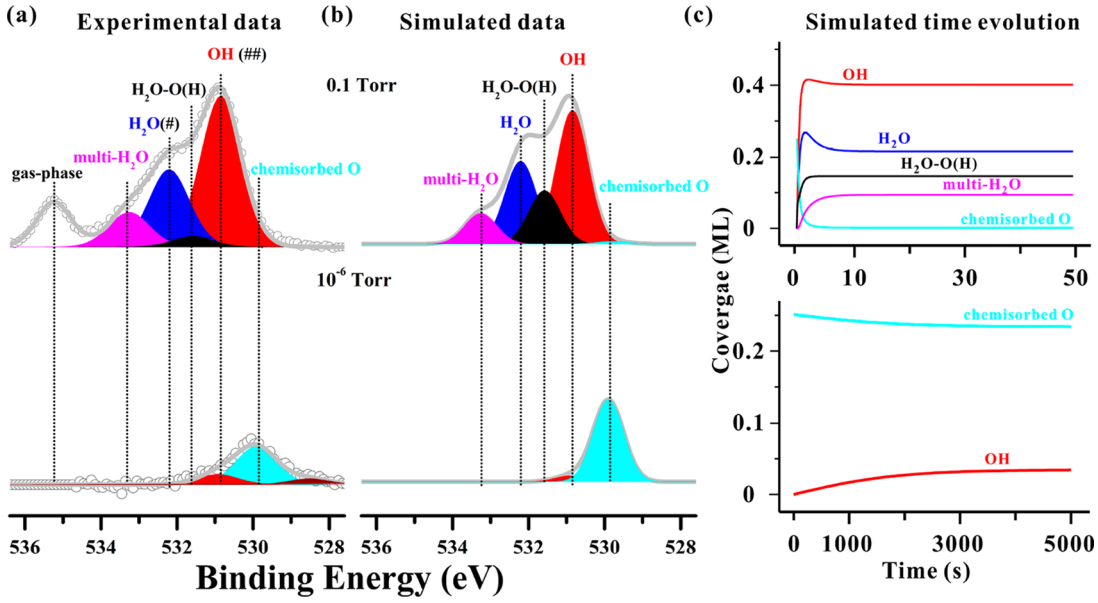

Figure 2. Predicted XPS spectrum vs experimentally observed spectrum under two extreme conditions. (a) Experimentally observed and (b) DFT simulated O 1s spectra with 0.1 Torr and 10^{-6} Torr H_2O adsorbed on Ag surface. (c) Time evolution of species' concentration predicted by CRN. Color code is the same throughout this paper: O* is blue, OH* is red, H_2O*--hb is black, H_2O* is blue, and multilayer water is magenta. The overall signal is depicted using a gray line. The initial O* concentration is fixed, and is estimated to be $^1/_4$ ML. The top row is the high water pressure condition (0.1 Torr), whereas the bottom row is low water pressure (10^{-6} Torr). Under high-pressure condition, O* is quickly consumed and OH* became the dominate species, whereas under low-pressure condition, only a fraction of O* is consumed. Although the effect is small, there is a possibility of contamination of CO_xH_y species showing up on Ag surface. In this work, the contribution from possible carbon contamination is labeled by # and ## in the figure. A detailed analysis explaining the scale of such contamination is included in the Supporting Information.

desorption

$$OH^* + H_2O^*\text{---hb} \rightarrow OH^* + H_2O_g,$$
$$G_1 = 0.14\ \text{eV},\ \ \mathbf{G_2 = -0.16\ eV} \tag{8}$$

desorption

$$O^* + H_2O^*\text{---hb} \rightarrow O^* + H_2O_g,$$
$$G_1 = 0.28\ \text{eV},\ \ G_2 = \mathbf{-0.02\ eV} \tag{9}$$

adsorption

$$OH^* + H_2O^*\text{---hb} + H_2O_g \rightarrow OH^* + \text{multilayer } H_2O,$$
$$\mathbf{G_1 = -0.02\ eV},\ \ G_2 = 0.29\ \text{eV} \tag{10}$$

desorption

$$OH^* + \text{multilayer } H_2O \rightarrow OH^* + H_2O^*\text{---hb} + H_2O_g,$$
$$G_1 = 0.01\ \text{eV},\ \ \mathbf{G_2 = -0.29\ eV} \tag{11}$$

reaction

$$2OH^* \rightarrow O^* + H_2O^*\text{---hb},$$
$$G_1 = 0.32\ \text{eV},\ \ G_2 = 0.32\ \text{eV} \tag{12}$$

We consider this CRN to include all possible initial steps of H_2O adsorption. Direct desorption of $O^* + O^* \rightarrow O_2$ is not included in the current CRN, because its barrier is reported to be 43.1 kcal/mol (1.87 eV).[36] Direct dissociation of $H_2O^* \rightarrow OH^* + H^*$ and $OH^* \rightarrow O^* + H^*$ are not included in the current CRN because their barriers are reported to be 1.80 eV, and 2.40 eV[37] respectively, which are orders of magnitude slower than all the presented reactions considered in current CRN (all within 0.5 eV).

The lack of water experimental data on Ag (111) is a known issue, as stated in ref 38: "Experimental characterization of H_2O monomer adsorption is exceedingly difficult, complicated by facile H_2O cluster formation. Cluster formation is problematic because it masks the true H_2O−metal interaction, making it difficult to make definitive statements about H_2O−metal bonding." On the other hand, we found high-quality calorimetry data of water splitting on Pt (111).[39] We expect the standard temperature pressure ΔG to be similar. The experiments concluded that the enthalpy for water splitting (activated by surface oxygen O*) is 57.4 and 60.2 kJ/mol (0.57 and 0.60 eV respectively for 2:1 and 3:1 H_2O-to-O* ratio), which is a fairly good comparison with the values we have here (0.74 and 0.67 eV respectively).

3.3. Direct Comparison of Theory and Experiment. To validate our protocol, we used two extreme pressure conditions (0.1 and 10^{-6} Torr) for H_2O adsorption on Ag(111) surface. Direct comparison of theory and experiment is in Figure 2.

The results can be explained in terms of the chemistry. At high pressure (0.1 Torr), the dominant chain reactions are

$$O^* + H_2O_g + * \rightarrow O^* + H_2O^*\text{---hb} \tag{1}$$

followed by

$$O^* + H_2O^*\text{---hb} \rightarrow 2OH^* \tag{3}$$

This surface OH* can then stabilize additional gas-phase H_2O and multilayer H_2O, as in

$$OH^* + H_2O_g + * \rightarrow OH^* + H_2O^* \tag{2}$$

$$OH^* + H_2O^*\text{---hb} + H_2O_g \rightarrow OH^* + \text{multilayer } H_2O \tag{10}$$

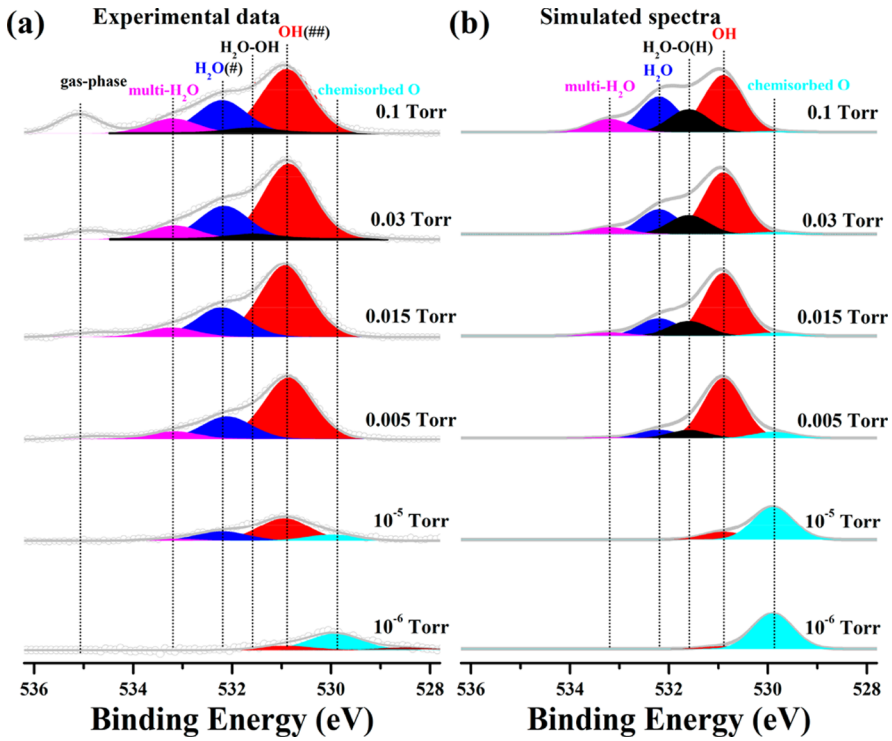

Figure 3. Comparison of experiment XPS spectrum and theory spectrum under isothermal condition at 298 K. the pressure increases gradually from bottom row to top row. In the low-pressure region (below ~10^{-5} Torr), chemisorbed O* is dominant and some amount of OH* is observed; in the more interesting high-pressure region (~10^{-3}–1 Torr), all oxygen-containing species are present except for chemisorbed O*. Both experiment and theory show the same trend for all species, as discussed in text.

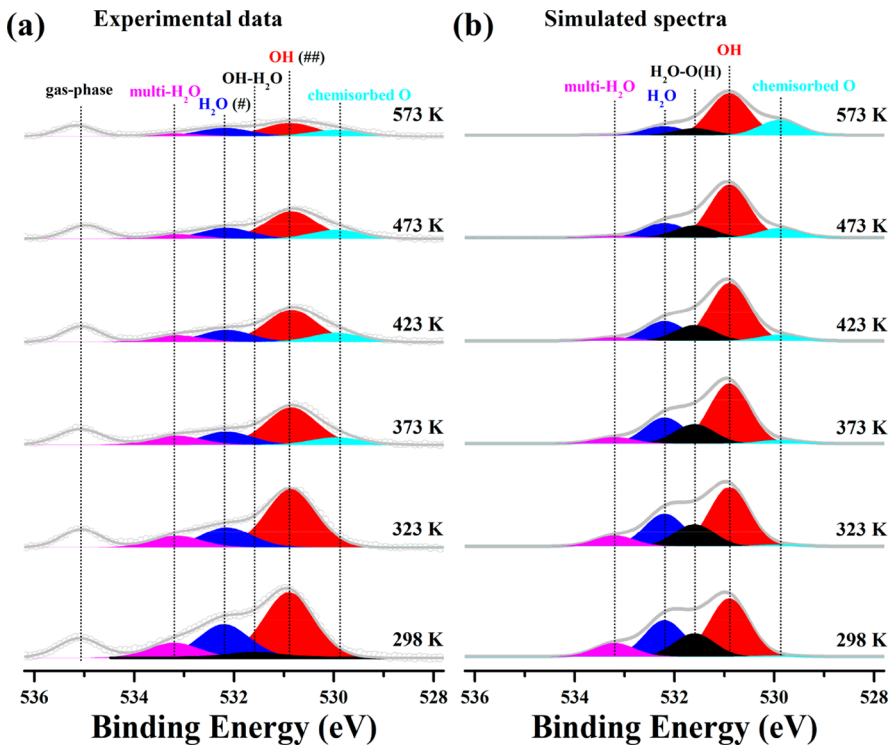

Figure 4. Comparison of experiment XPS and theory spectra under isobaric condition at 0.1 Torr. The temperature increases gradually from the bottom to the top. Both experiment and theory show appearance of O* around 373–423 K, while all other species decrease in their intensity as temperature increases.

Assuming the initial surface concentration of O* is sufficiently dilute ($^{1}/_{4}$ ML) that the above product species can be accommodated, all O* should be consumed, so that the O* peak (blue) would be undetectable, as observed. Instead, strong OH* (red), moderate H_2O*, H_2O*---hb, and multilayer H_2O* peaks are detected.

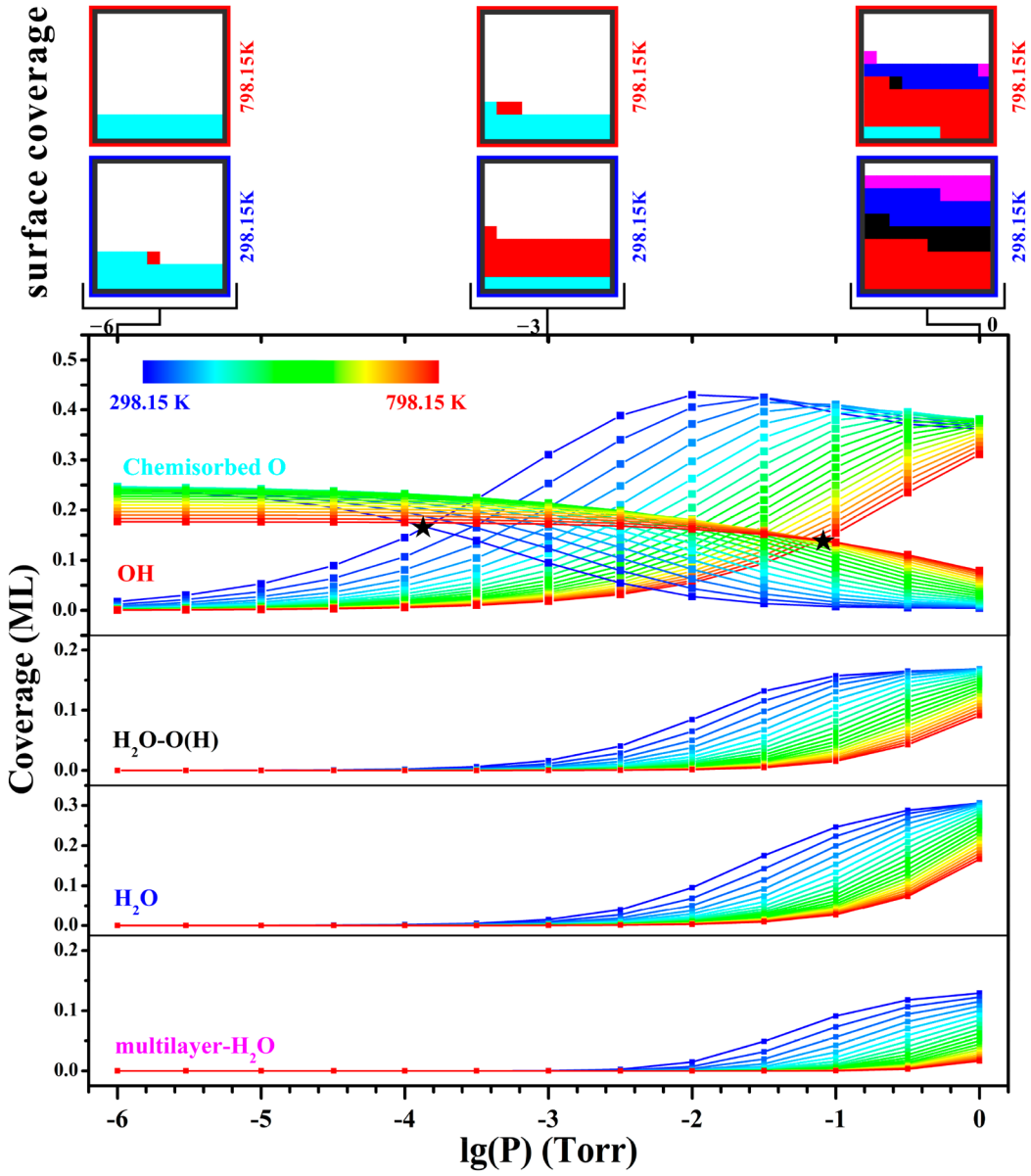

Figure 5. Overall landscape of oxygen-containing species, predicted using QM and CRN. The relative concentration of each species at every pressure (from 10^{-6} Torr to 1 Torr) and temperature (from 298.15 to 798.15 K) are shown. The star sign shows the transition from the O*-rich region to the OH*-rich region, which is shifted to higher pressure as temperature increases. The surface coverage section provides direct visualization of the populations for different species. The maximum coverage 1 ML is depicted as the big 10×10 box as the drawing board, and thus every 0.01 ML is a small square within the drawing board. To directly show the concentration of every species, we colored the small boxes accordingly. The color code is consistent with other figures: O* is blue, OH* is red, H_2O*---hb is black, H_2O* is blue, and multilayer water is magenta.

Under low pressure (10^{-6} Torr), the chemistry is different:

$$O^* + H_2O_g + * \leftrightarrow O^* + H_2O^*\text{---hb} \quad (1)$$

is in equilibrium. Although reaction

$$O^* + H_2O^*\text{---hb} \rightarrow 2OH^* \quad (3)$$

is exoenergetic, the equilibrium would have a fraction of surface O* binding to H_2Og to convert into OH* via (1) and (3). As a result, strong O* and weak OH* peaks are detected. Extrapolated from the low-pressure regime XPS data, the O* concentration is estimated to be $^1/_4$ ML. Note that we are not able to compare directly the population of gas-phase H_2O (white) because the volume of the gas phase probed by XPS is uncertain. The relative concentration for all species are in good agreement with experiment.

3.4. Predictions as a Function of Pressure and Temperature. *3.4.1. Isotherm Condition at 298 K.* Pressure plays two major roles in the kinetics:

(1) Increased pressures of H_2O_g increase the total amount of H_2O and products on the surface ($pV = nRT$). Collision frequency increases as well, where the flux of particles impinging on the surface is given by $f_s = p/\sqrt{2\pi m k_B T}$.

(2) The entropy term depends on pressure by $RT\ln(P_2/P_1)$, so that the free energy for reactions involving adsorption and desorption are pressure-dependent.

As shown in Figure 3b), we predict that there are two regions of interest:

- the low-pressure region (below $\sim 10^{-5}$ Torr), where chemisorbed O* is dominant and some amount of OH* is observed
- a more interesting high-pressure region ($\sim 10^{-3}$–1 Torr), where all oxygen-containing species are present except for chemisorbed O*

The dominant species in the high-pressure region is OH*. This is further validated in the experimental data shown in Figure 3a).

Both experiment and theory arrive at the same trend for all species, which are summarized as OH* coverage increases until ~10 mTorr and then decreases because of site constraint, as shown in (3), where two adjacent sites are required for the production of OH*. H_2O*, H_2O*---hb, and multilayer H_2O* coverages increase as pressure increases; of these, H_2O coverage increases at the fastest speed.

3.4.2. Isobar Condition at 0.1 Torr. Temperature also plays two major roles in the kinetics:

(1) The rotational, vibrational, and translational entropy term depends on temperature, as calculated in Jaguar Maestro.

(2) The exponential part of the rate constant, $K = k_B \frac{T}{h} \exp\left(\frac{dG}{k_B T}\right)$, is most sensitive to the temperature for all 12 reactions involved in the CRN.

Figure 4b shows that we predict a non-negligible amount of chemisorbed O* starts to appear at around 423 K, whereas all other species, such as multilayer H_2O*, H_2O*, and OH-H_2O*, desorb to significantly decrease the signal, in general agreement with the experiment shown in Figure 4a). The only small discrepancy is that OH* was observed to decrease quickly experimentally, whereas theory does not show such a dramatic decrease, although some decrease is found at higher temperature (see Figure 5, below). A detailed discussion of possible sources of discrepancy and future direction can be found in the Conclusion section.

3.4.3. Overall Landscape. Figure 5 shows our predictions across a wide range of temperature and pressure, from 298 to 737 K and from 10^{-6} to 1 Torr. We find a high-pressure region in which all species exist except O*, and a low-pressure region, having strong O* signal and moderate OH* signals. We report that this transition point moves to the right side (higher pressure side) as temperature increases, marked using the star sign in Figure 5. This is mostly because reaction 3 is exothermic, so that more O* would be present at higher temperature. O* and OH* are arguably the most important intermediates in this system, since they further determine the concentrations of H_2O*, H_2O---hb, and multilayer H_2O* as reactions 1, 2, and 10 proceed. At every T/P grid in Figure 5, we can visualize the relative concentration of all oxygen-containing species.

4. CONCLUSION

We present here the details of how H_2O interacts initially with the Ag(111) surface, predicting the free energy and kinetics to determine the concentration profile of five oxygen-containing surface species across a wide range of pressure and temperature (pressure from 10^{-6} to 1 Torr, and temperature from 298 to 798 K). These results explain the role of O* and OH* as important intermediates, showing how the concentration of each species is closely connected to those of all other oxygen-containing surface species, and matching available data from the APXPS experiments. The constraint in the kinetic model is that every species's concentration is bounded by 0 and 1 ML. In terms of the concentration profile, we found that even at pressure as low as 0.1 Torr, the surface coverage is quite high, and saturation is observed from 0.03 to 1 Torr. After saturation is reached, there is still a small area that is uncovered. H_2O alone does not split to OH* and O* automatically, but with the promotion of OH* and O*, this splitting is observed. This is consistent with the previously reported non-wetting behavior of the Ag(111) surface.[38,40]

Due to the novelty of the current CRN approach, the discussion of possible discrepancies with respect to experimental data is very open. In general, there are several directions (higher order approximations and corrections) for future work in this field:

(1) The energetic term as well as kinetic constants term would no longer be a "constant" but rather dynamic. As coverage increases, kinetic constants could be explicitly extrapolated from the different geometry. This requires a significant amount of extra calculation and correction to be made. Thus, for the reaction A + B → C, $\frac{d[C]t}{dt} = [A]t[B]tK$, then K would be dependent on $[A]t$, $[B]t$, and even $[C]t$ at the same time, which may need to be solved self-consistently. This would increase the computational effort extensively, but this would explain why a more crowded species such as H_2O–OH is over-stabilized, because it should have felt the repulsion of surroundings more when the concentration is higher (Figure 2, high-pressure case).

(2) A specific CRN model targeted to the surface could be developed, meaning that surface sites will be taken into consideration to differentiate the top site of H_2O*, the fcc site of OH*, O*, etc. The current CRN model can be classified as bulk CRN, where the concentration of product is only dependent on the concentration of reactants, and it is acceptable for adsorption/desorption between gas-/liquid-phase molecules and surface. However, in a surface-CRN scheme, a surface reaction such as O* + H_2O---hb → OH* + OH* would happen only when species are adsorbed explicitly on neighboring sites and when two adjacent three-fold sites for the OH* are available. Thus, the current CRN model could predict an OH* population higher than reality.

(3) Contamination, such as with hydrogen and carbon, is possible. Hydrogen could react with surface OH, forming H_2O and desorbing easily at high temperature, but hydrogen complicates the issue because it cannot be directly observed in XPS. On the other hand, possible carbon contamination can be analyzed by analyzing the C 1s signal, as discussed in the Supporting Information.

Combining QM free energy, QM core-level shift, CRN kinetics, and XPS experimental data, we demonstrate a procedure to provide an atomic description compatible with the macroscopic observables. Theory and experiment are intertwined closely to provide a chemical understanding in both qualitative and quantitative agreements. We demonstrate the SANDS protocol that provides a robust interpretation from the theory side, which is cross-validated against experimental data. Because of its fundamental grounding in thermodynamics and kinetic theory, this method should be applicable to a broad variety of surface systems of interest.

AUTHOR INFORMATION

Corresponding Authors

*wag@caltech.edu (W.A.G.).
*ejcrumlin@lbl.gov (E.J.C.).
*jyano@lbl.gov (J.Y.).

ORCID

Jin Qian: 0000-0002-0162-0477
Junko Yano: 0000-0001-6308-9071
Ethan J. Crumlin: 0000-0003-3132-190X
William A. Goddard, III: 0000-0003-0097-5716

Author Contributions

#J.Q. and Y.Y. contributed equally.

Notes

The authors declare no competing financial interest.

ACKNOWLEDGMENTS

We thank Yufeng Huang and Samuel Clamons for helpful discussions. This project was supported by the Joint Center for Artificial Photosynthesis, a DOE Energy Innovation Hub, supported through the Office of Science of the U.S. Department of Energy under Award No. DE-SC0004993. W.A.G. was supported by the Computational Materials Sciences Program funded by the U.S. Department of Energy, Office of Science, Basic Energy Sciences, under Award No. DE-SC00014607. The calculations were carried out on the Extreme Science and Engineering Discovery Environment (XSEDE), which is supported by National Science Foundation Grant No. ACI-1548562. This research used resources of the Advanced Light Source, which is a DOE Office of Science User Facility under contract no. DE-AC02-05CH11231. In addition, Y.Y. and E.J.C. were partially supported by an Early Career Award in the Condensed Phase and Interfacial Molecular Science Program, in the Chemical Sciences Geosciences and Biosciences Division of the Office of Basic Energy Sciences of the U.S. Department of Energy under Contract No. DE-AC02-05CH11231.

REFERENCES

(1) Favaro, M.; Xiao, H.; Cheng, T.; Goddard, W. A.; Yano, J.; Crumlin, E. J. Subsurface Oxide Plays a Critical Role in CO2 Activation by Cu(111) Surfaces to Form Chemisorbed CO2, the First Step in Reduction of CO2. *Proc. Natl. Acad. Sci. U. S. A.* **2017**, *114* (26), 6706−6711.

(2) Xiao, H.; Cheng, T.; Goddard, W. A.; Sundararaman, R. Mechanistic Explanation of the PH Dependence and Onset Potentials for Hydrocarbon Products from Electrochemical Reduction of CO on Cu (111). *J. Am. Chem. Soc.* **2016**, *138* (2), 483−486.

(3) Hoshi, N.; Mizumura, T.; Hori, Y. Significant Difference of the Reduction Rates of Carbon Dioxide between Pt(111) and Pt(110) Single Crystal Electrodes. *Electrochim. Acta* **1995**, *40* (7), 883−887.

(4) Luc, W.; Collins, C.; Wang, S.; Xin, H.; He, K.; Kang, Y.; Jiao, F. Ag−Sn Bimetallic Catalyst with a Core−Shell Structure for CO2 Reduction. *J. Am. Chem. Soc.* **2017**, *139* (5), 1885−1893.

(5) Cheng, T.; Huang, Y.; Xiao, H.; Goddard, W. A. Predicted Structures of the Active Sites Responsible for the Improved Reduction of Carbon Dioxide by Gold Nanoparticles. *J. Phys. Chem. Lett.* **2017**, *8* (14), 3317−3320.

(6) Reier, T.; Oezaslan, M.; Strasser, P. Electrocatalytic Oxygen Evolution Reaction (OER) on Ru, Ir, and Pt Catalysts: A Comparative Study of Nanoparticles and Bulk Materials. *ACS Catal.* **2012**, *2* (8), 1765−1772.

(7) Ping, Y.; Nielsen, R. J.; Goddard, W. A. The Reaction Mechanism with Free Energy Barriers at Constant Potentials for the Oxygen Evolution Reaction at the IrO2 (110) Surface. *J. Am. Chem. Soc.* **2017**, *139* (1), 149−155.

(8) Bunluesin, T.; Gorte, R. J.; Graham, G. W. Studies of the Water-Gas-Shift Reaction on Ceria-Supported Pt, Pd, and Rh: Implications for Oxygen-Storage Properties. *Appl. Catal., B* **1998**, *15* (1), 107−114.

(9) Gokhale, A. A.; Dumesic, J. A.; Mavrikakis, M. On the Mechanism of Low-Temperature Water Gas Shift Reaction on Copper. *J. Am. Chem. Soc.* **2008**, *130* (4), 1402−1414.

(10) Ikemiya, N.; Gewirth, A. A. Initial Stages of Water Adsorption on Au Surfaces. *J. Am. Chem. Soc.* **1997**, *119* (41), 9919−9920.

(11) Cheng, T.; Xiao, H.; Goddard, W. A. Reaction Mechanisms for the Electrochemical Reduction of CO2 to CO and Formate on the Cu(100) Surface at 298 K from Quantum Mechanics Free Energy Calculations with Explicit Water. *J. Am. Chem. Soc.* **2016**, *138* (42), 13802−13805.

(12) Thiel, P.; Madey, T. The Interaction of Water with Solid Surfaces: Fundamental Aspects. *Surf. Sci. Rep.* **1987**, *7* (6−8), 211−385.

(13) Lipkowski, J.; Ross, P. N. *Structure of Electrified Interfaces*; VCH Publishers, 1993.

(14) Kay, B. D.; Lykke, K. R.; Creighton, J. R.; Ward, S. J. The Influence of Adsorbate−Absorbate Hydrogen Bonding in Molecular Chemisorption: NH3, HF, and H2O on Au(111). *J. Chem. Phys.* **1989**, *91* (8), 5120−5121.

(15) Smith, R. S.; Huang, C.; Wong, E. K. L.; Kay, B. D. Desorption and Crystallization Kinetics in Nanoscale Thin Films of Amorphous Water Ice. *Surf. Sci.* **1996**, *367* (1), L13−L18.

(16) Löfgren, P.; Ahlström, P.; Chakarov, D.; Lausmaa, J.; Kasemo, B. Substrate Dependent Sublimation Kinetics of Mesoscopic Ice Films. *Surf. Sci.* **1996**, *367* (1), L19−L25.

(17) Heras, J.; Viscido, L. Work Function Changes upon Water Contamination of Metal Surfaces. *Appl. Surf. Sci.* **1980**, *4* (2), 238−241.

(18) Atkinson, S. J.; Brundle, C. R.; Roberts, M. W. Ultra-Violet and X-Ray Photoelectron Spectroscopy (UPS and XPS) of CO, CO2, O2 and H2O on Molybdenum and Gold Films. *Faraday Discuss. Chem. Soc.* **1974**, *58* (0), 62−79.

(19) Brundle, C. R.; Roberts, M. W. Surface Sensitivity of He I Photoelectron Spectroscopy (UPS) for H2O Adsorbed on Gold. *Surf. Sci.* **1973**, *38* (1), 234−236.

(20) Powell, C. J.; Jablonski, A.; Salvat, F.; Lee, A. Y. *NIST Electron Elastic-Scattering Cross-Section Database, Version 4.0*; User's Guide, NIST NSRDS 64; National Institute of Standards and Technology, 2016; https://doi.org/10.6028/NIST.NSRDS.64.

(21) Kresse, G.; Furthmüller, J. Efficient Iterative Schemes for Ab Initio Total-Energy Calculations Using a Plane-Wave Basis Set. *Phys. Rev. B: Condens. Matter Mater. Phys.* **1996**, *54* (16), 11169−11186.

(22) Johnson, E. R.; Becke, A. D. A Post-Hartree-Fock Model of Intermolecular Interactions: Inclusion of Higher-Order Corrections. *J. Chem. Phys.* **2006**, *124* (17), 174104.

(23) Grimme, S.; Antony, J.; Ehrlich, S.; Krieg, H. A Consistent and Accurate Ab Initio Parametrization of Density Functional Dispersion Correction (DFT-D) for the 94 Elements H-Pu. *J. Chem. Phys.* **2010**, *132* (15), 154104.

(24) Kittel, C. *Introduction to Solid State Physics*; Wiley, 2005.

(25) Mercurio, G.; McNellis, E. R.; Martin, I.; Hagen, S.; Leyssner, F.; Soubatch, S.; Meyer, J.; Wolf, M.; Tegeder, P.; Tautz, F. S.; et al. Structure and Energetics of Azobenzene on Ag(111): Benchmarking Semiempirical Dispersion Correction Approaches. *Phys. Rev. Lett.* **2010**, *104* (3), No. 036102.

(26) Bochevarov, A. D.; Harder, E.; Hughes, T. F.; Greenwood, J. R.; Braden, D. A.; Philipp, D. M.; Rinaldo, D.; Halls, M. D.; Zhang, J.; Friesner, R. A. Jaguar: A high-performance quantum chemistry software program with strengths in life and materials sciences. *Int. J. Quantum Chem.* **2013**, *113* (18), 2110−2142.
(27) Sprowl, L. H.; Campbell, C. T.; Árnadóttir, L. Hindered Translator and Hindered Rotor Models for Adsorbates: Partition Functions and Entropies. *J. Phys. Chem. C* **2016**, *120* (18), 9719−9731.
(28) Craciun, G.; Feinberg, M. Multiple Equilibria in Complex Chemical Reaction Networks: II. The Species-Reaction Graph. *SIAM J. Appl. Math.* **2006**, *66* (4), 1321−1338.
(29) Chen, Y.-J.; Dalchau, N.; Srinivas, N.; Phillips, A.; Cardelli, L.; Soloveichik, D.; Seelig, G. Programmable Chemical Controllers Made from DNA. *Nat. Nanotechnol.* **2013**, *8* (10), 755−762.
(30) Angeli, D. A Tutorial on Chemical Reaction Network Dynamics. *Eur. J. Control* **2009**, *15* (3), 398−406.
(31) Soloveichik, D.; Cook, M.; Winfree, E.; Bruck, J. Computation with Finite Stochastic Chemical Reaction Networks. *Nat. Comput.* **2008**, *7* (4), 615−633.
(32) Grass, M. E.; Karlsson, P. G.; Aksoy, F.; Lundqvist, M.; Wannberg, B.; Mun, B. S.; Hussain, Z.; Liu, Z. New Ambient Pressure Photoemission Endstation at Advanced Light Source Beamline 9.3.2. *Rev. Sci. Instrum.* **2010**, *81* (5), No. 053106.
(33) Li, W.-X.; Stampfl, C.; Scheffler, M. Subsurface Oxygen and Surface Oxide Formation at Ag(111): A Density-Functional Theory Investigation. *Phys. Rev. B: Condens. Matter Mater. Phys.* **2003**, *67* (4), No. 045408.
(34) Bao, X.; Lehmpfuhl, G.; Weinberg, G.; Schlögl, R.; Ertl, G. Variation of the Morphology of Silver Surfaces by Thermal and Catalytic Etching. *J. Chem. Soc., Faraday Trans.* **1992**, *88* (6), 865−872.
(35) Phatak, A. A.; Delgass, W. N.; Ribeiro, F. H.; Schneider, W. F. Density Functional Theory Comparison of Water Dissociation Steps on Cu, Au, Ni, Pd, and Pt. *J. Phys. Chem. C* **2009**, *113* (17), 7269−7276.
(36) Campbell, C. T. Atomic and Molecular Oxygen Adsorption on Ag(111). *Surf. Sci.* **1985**, *157* (1), 43−60.
(37) Wang, S.; Petzold, V.; Tripkovic, V.; Kleis, J.; Howalt, J. G.; Skúlason, E.; Fernández, E. M.; Hvolbæk, B.; Jones, G.; Toftelund, A.; et al. Universal Transition State Scaling Relations for (de)-Hydrogenation over Transition Metals. *Phys. Chem. Chem. Phys.* **2011**, *13* (46), 20760−20765.
(38) Michaelides, A. Density Functional Theory Simulations of Water−Metal Interfaces: Waltzing Waters, a Novel 2D Ice Phase, and More. *Appl. Phys. A: Mater. Sci. Process.* **2006**, *85* (4), 415−425.
(39) Lew, W.; Crowe, M. C.; Campbell, C. T.; Carrasco, J.; Michaelides, A. The Energy of Hydroxyl Coadsorbed with Water on Pt(111). *J. Phys. Chem. C* **2011**, *115* (46), 23008−23012.
(40) Tonigold, K.; Gross, A. Dispersive Interactions in Water Bilayers at Metallic Surfaces: A Comparison of the PBE and RPBE Functional Including Semiempirical Dispersion Corrections. *J. Comput. Chem.* **2012**, *33* (6), 695−701.